A. Pournaghshband, S. Afshan and A. S. J. Foster. (2019) Structural fire performance of axially and rotationally restrained stainless steel columns. *Thin-Walled Structures*; **137**: 561–572.

Structural fire performance of axially and rotationally restrained stainless steel columns

A. Pournaghshband [a], S. Afshan [a*] and A. S. J. Foster [b]
[a] Brunel University London, UK
[b] The University of Manchester, UK

*Corresponding author E-mail: Sheida.Afshan@brunel.ac.uk

Abstract

This paper describes a step improvement in the numerical modelling of the structural response of axially and rotationally restrained stainless steel columns at elevated temperatures. The developed finite element models form a sequentially coupled thermal stress analysis that comprises a heat transfer model, a buckling analysis, and a geometrically and materially non-linear stress analysis. The proposed finite element methodology is more sophisticated than any other reported attempts to model the fire response of structural stainless steel that take into account influence of adjoining members. A high degree of predictive accuracy is achieved, with the developed models on average predicting the failure temperatures and times of test specimens reported in the literature within 2% and 6%, respectively. A parametric study is performed that investigates the influence of axial restraint stiffness, rotational restraint stiffness, column slenderness and load level. It is shown that while increasing axial restraint stiffness reduces the failure temperature of stainless steel columns in fire, increasing rotational restraint stiffness has the opposite effect. The methodology and results of this paper will provide both a tool for practice and a suite of results that can be extended to develop the existing and currently limited codified approaches to structural stainless steel design.

Keywords: Axial restraint; Column, Fire; Numerical modelling; Rotational restraint; Stainless steel.

1. Introduction

Stainless steel has become an integral part of the built environment, finding applications in a wide range of structural and architectural elements, particularly in challenging environments, such as coastal structures, tunnels and industrial structures, taking advantage of its excellent corrosion resistance, durability and favourable mechanical properties [1]. With greater emphasis placed on the whole life-cycle costs, rather than initial expenditure, and sustainability, stainless steel, with its intrinsic durability and high potential for reuse and recycling, has become a viable alternative material for several areas of construction. However, stainless steel structural members are often used unprotected for aesthetic and architectural reasons, and need to demonstrate sufficient fire resistance when used in applications where fire is a significant hazard.

In recognition of the many desirable properties of stainless steel, recent years have seen significant research into the response of structural stainless steel components, enabling the development and expansion of design codes and specifications worldwide [2-5]. Despite considerable progress in the publication of design guidelines for stainless steel at room

temperature, design rules for stainless steel structures exposed to elevated temperatures are limited. Stainless steel generally displays superior strength and stiffness retention at elevated temperature when compared to carbon steel, especially at the important temperature range of 500-800 °C, but also exhibits greater thermal expansion and lower thermal conductivity [6-7]. The combined effects of these factors need to be systematically accounted for in the analysis and design of stainless steel structures in fire. Figure 1(a) shows the strength reduction factor $k_{0.2,\theta}$, defined as the elevated temperature 0.2% proof stress $f_{0.2,\theta}$ normalized by the room temperature 0.2% proof stress $f_{0.2}$, for austenitic EN 1.4571, duplex EN 1.4462 and ferritic EN 1.4003 stainless steel grades from [8] and carbon steel from [9]. The stiffness retention factor $k_{E,\theta}$, defined as the elevated temperature initial tangent modulus E_θ normalized by the initial tangent modulus at room temperature E, for stainless steel and carbon steel are shown in Figure 1(b).

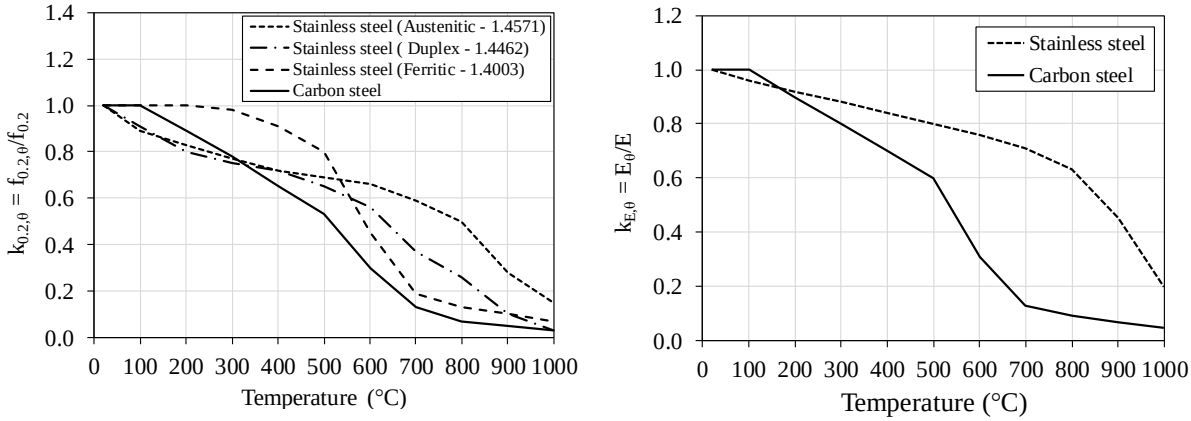

(a) Variation of strength with temperature. (b) Variation of stiffness with temperature.

Figure 1: Strength and stiffness retention of stainless steel and carbon steel at elevated temperatures.

The assessment of the adequacy of stainless steel structures in fire in current design standards, e.g. EN 1993-1-4 [2] and EN 1993-1-2 [9], is mainly based on the performance of isolated structural elements in standard furnace tests. Experimental and numerical studies of stainless steel structures reported in the literature also relate to individual elements such as statically determinate simply supported compression and flexural elements in fire [10-11]. It is well established that such investigations are of limited relevance in the analysis of whole frame structural behaviour, where in addition to the degradation of material strength and stiffness at elevated temperature, thermally induced stresses, from restrained thermal expansion and thermal bowing effects, govern the structural response [12]. Furthermore, the redundancy in structural frames allows alternative load paths as well as additional load resisting mechanisms to develop in fire, enabling structures to continue supporting the applied loading when the strength has been exceeded at a single location [12-13]. In structural frames, columns are both axially and rotationally restrained by their adjoining unheated members. It has been shown that while rotational restraint has a beneficial effect on the fire resistance of steel columns, the influence of axial restraint is rather detrimental due to the additional thermally-induced axial stresses that can initiate buckling and yielding [12-13]. Therefore, to understand the realistic

performance of stainless steel columns in fire, it is essential to consider the axial and rotational restraints by the adjacent structural members.

In the present paper, the performance of axially and rotationally restrained stainless steel columns in fire is investigated through an extensive numerical modelling study. The development of the numerical models and their validation against existing experimental results are described in Section 2. Numerical parametric studies carried out to investigate the effect of key parameters including: (i) axial restraint stiffness; (ii) rotational restraint stiffness; (iii) column slenderness; and (iv) load level on the performance of restrained stainless steel columns are presented in Section 3. The analysis of the obtained numerical results and discussion thereof are presented in Section 4.

2. Development and validation of numerical models

Numerical analyses were carried out using the non-linear finite element analysis package ABAQUS, version 2016 [14] to simulate the response of axially and rotationally restrained stainless steel columns in fire. The numerical models were first validated against existing experimental results of axially and rotationally restrained carbon steel column tests [15], and were subsequently used to perform a series of parametric studies on stainless steel columns. The development of the finite element (FE) models and their validation are presented herein while the results of the parametric studies and discussions thereof are described in Section 3.

2.1. Test results from literature

In the absence of fire tests on restrained stainless steel columns, the finite element models were validated against the restrained carbon steel tests reported by Correia and Rodrigues [15]. The tests were carried out in the Materials and Structures Laboratory at University of Coimbra. A summary of the tests, including the nominal section size, non-dimensional minor axis member slenderness $\bar{\lambda}$, applied initial axial load P_0, axial restraint stiffness ratio α_A, rotational restraint stiffness ratio α_R and the measured yield strength of the material f_y is reported in Table 1.

The tested specimens were HEA 160 and HEA 200 of grade S355. The columns were all of nominal length L_0 = 3m. Two different load levels were applied to each column specimen: 30% and 70% of the room temperature minor axis buckling resistance $N_{b,Rd,z}$, determined in accordance with EN 1993-1-2 [9]. Owing to the adopted test set-up, the non-dimensional slenderness $\bar{\lambda}$, reported in Table 1, was calculated using an effective length of 0.7L, where L was taken as the length of the column L_0 (3m) plus the restraining force measurement device (0.6m) as adopted by the authors [15].

The axial restraint stiffness ratio α_A is defined as the ratio of the axial stiffness of the surrounding structure k_A to the axial stiffness of the column $k_{A,C}$, Equation (1). The measured axial restraint stiffness values of the restraining frame at room temperature were 13, 45 and 128 kN/mm. Similarly, the rotational restraint stiffness ratio α_R is defined as the ratio of the rotational stiffness of the surrounding structure k_R to the rotational stiffness of the column $k_{R,C}$, Equation (2). In Equations (1) and (2), A_C and I_C are the cross-sectional area and second moment of area of the restrained column, respectively, and E_C is the Young's modulus of the material at room temperature.

$$\alpha_A = \frac{k_A}{k_{A,C}} \quad , \quad k_{A,C} = \frac{A_C.E_C}{L_0} \tag{1}$$

$$\alpha_R = \frac{k_R}{k_{R,C}} \quad , \quad k_{R,C} = \frac{4E_C.I_C}{L_0} \tag{2}$$

Table 1: Summary of the restrained carbon steel columns tests carried out by Correia and Rodrigues [15].

Specimen reference	$\bar{\lambda}$	P_0 (kN)	α_A	α_R	f_y
HEA200-K13-L70	0.67	999.8	0.035	1.290	364
HEA160-K13-L70	0.88	621.0	0.048	2.801	399
HEA200-K13-L30	0.68	428.0	0.035	1.290	375
HEA160-K13-L30	0.88	266.0	0.048	2.801	399
HEA160-K45-L70	0.88	621.0	0.166	3.262	399
HEA160-K45-L30	0.86	266.0	0.166	3.262	385
HEA200-K45-L70	0.67	999.8	0.119	1.503	360
HEA200-K45-L30	0.67	428.0	0.119	1.503	364
HEA200-K128-L30	0.71	428.0	0.341	2.097	412
HEA160-K128-L30	0.87	266.0	0.473	4.551	395
HEA200-K128-L70	0.71	999.8	0.341	2.097	412
HEA160-K128-L70	0.87	621.0	0.473	4.551	395

All fire tests were performed anisothermally, whereby the load was applied at room temperature and maintained at a constant level while the temperature was increased, following the standard ISO-834 [9] fire curve, until failure. In order to assess the development of the internal member forces due to fire only, during the application of the axial load at room temperature, the columns had pin-ended boundary condition at both ends. Axial and rotational restraints were subsequently added in the later stage when the temperature was increased. The steel temperature was measured during the tests at five cross-sections along the length of the tested columns – sections S1-S5 in Figure 2(a) by means of a series of thermocouples attached at three locations in each section – T1-T3 in Figure 2(b) [15].

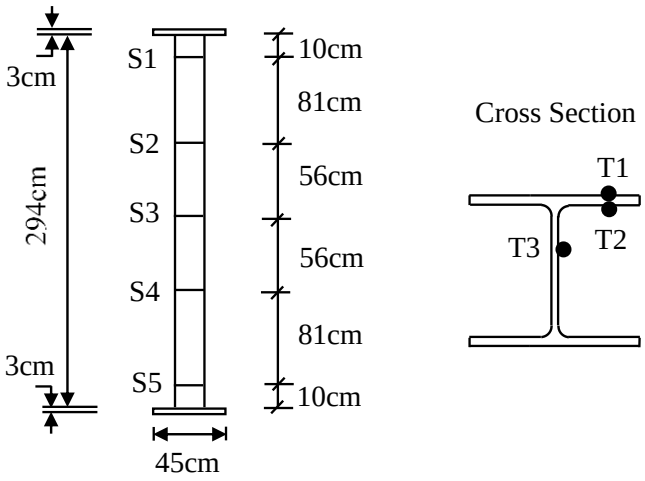

(a) Sections S1-S5. (b) Locations T1-T3.

Figure 2: Measured temperatures in the tested columns at (a) sections S1-S5 and (b) locations T1-T3 [15].

2.2 Description of the FE models

For each model, a sequentially coupled thermal-stress analysis was carried out, involving three types of numerical analyses – a heat transfer analysis to obtain the temperature development in the structural members, a linear elastic buckling analysis to determine the buckling mode shapes and finally a geometrically and materially non-linear stress analysis, which incorporated the temperature field from the heat transfer analysis and the buckling mode shapes as imperfections from the linear elastic buckling analysis. The development of the models for the test data in Table 1 are described hereafter.

2.2.1 Heat transfer model

Heat transfer analyses were carried out to obtain the evolution of the steel temperature with the fire exposure time for all the columns, which was required as input for the stress analysis part of the modelling procedure. The thermal analysis of a structural member can be divided into two parts: the heat transfer from the fire to the exposed surface of the structural element through combined convection and radiation heat transfer mechanisms, and conductive heat transfer within the structural member itself. The electric furnace used consisted of two 1m×1.5m×1.5m modules and one 0.5m×1.5m×1.5m module which were placed on top of each other over the central 2.5m of the tested columns. The top and bottom 250mm ends of the columns were unheated and were wrapped in isolation material – these parts were left unheated in the heat transfer analysis.

The measured furnace temperatures of each of the three modules were applied uniformly to the corresponding parts of the central 2.5m of the columns with a uniform initial temperature of 20°C. The measured furnace temperature was not reported for the HEA160-K128-L30 specimen; hence the standard ISO 834 temperature-time curve given in EN 1993-1-2 [9] was employed. The convective heat transfer coefficient and the emissivity factor were taken as 25 W/m^2K and 0.7, respectively, as specified in EN 1993-1-2 [9]. Other thermal properties including specific heat, thermal conductivity and thermal expansion given in EN 1993-1-2 [9]

were adopted. All steel columns were modelled by means of shell element DS4 with a uniform mesh size of 10mm×10mm, which based on the conducted mesh sensitivity analysis provided accurate results with practical computational times.

Figures 3(a) and 3(b) show the mean temperature (i.e. average of T1-T3) versus time results for sections S1-S5 obtained from the thermal analysis model for the HEA200-K13-L70 and HEA160-K45-L30 columns, respectively, which are in good agreement with the test measured results. The results from the heat transfer analysis, which consisted of the temperature distribution for all the nodes within the three-dimensional model, were stored as a function of time and subsequently read into the stress analysis model as a predefined field.

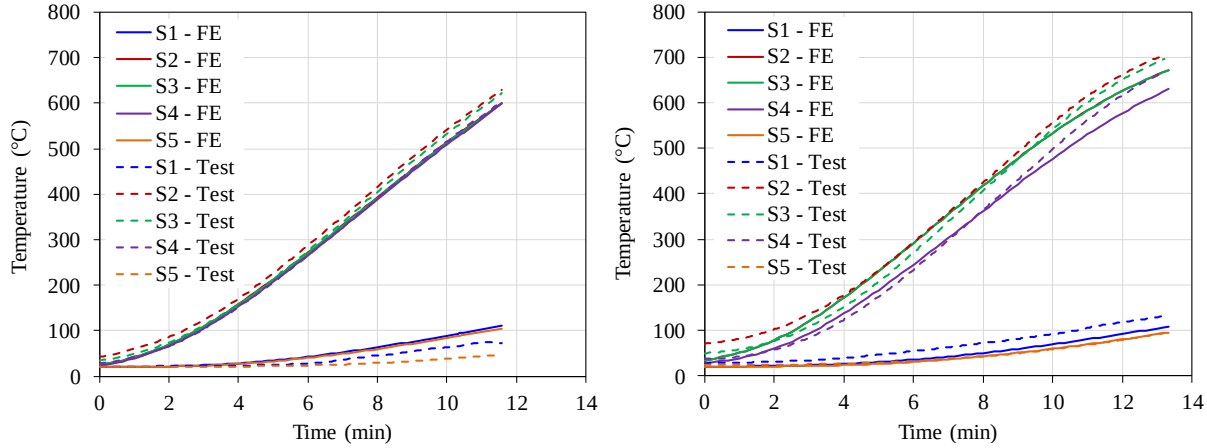

(a) HEA200-K13-L70. (b) HEA160-K45-L30.

Figure 3: Comparison of the time-temperature results from test and numerical models.

2.2.2 Stress analysis model

A stress analysis model was subsequently conducted, the details of which are described in this section. The simulated model of the axially and rotationally restrained columns is shown in Figure 4. The axial and rotational restraints provided by the adjacent structural elements were represented by axial and rotational springs, respectively. The axial and rotational springs were simulated by SPRING elements (*Element, type=Spring2 for axial springs and *Element, type=Spring1 for rotational springs). Both spring types were assumed to be linear elastic with axial stiffness k_A and rotational stiffness k_R. For the validation models, this assumption deemed acceptable since the restraining frame was placed outside the furnace during the tests and the applied surrounding structure stiffnesses did not change over the fire exposure time. Hence, the measured axial and rotational restraint stiffness values reported in Table 1 were directly assigned to the axial and rotational springs of the numerical models, respectively. In real structural frames, the axial and rotational restraints may in fact be nonlinear; this could be due to the degradation of material stiffness with temperature of the floor system and the large inelastic deflection of the surrounding structural elements [16-17]. The axial and rotational restraints have been assumed to be linear elastic in the models developed herein, as has also been adopted in a number of similar other studies [16-18], with the effects of different axial and rotational restraint stiffness being investigated in the subsequent parametric studies of stainless steel columns.

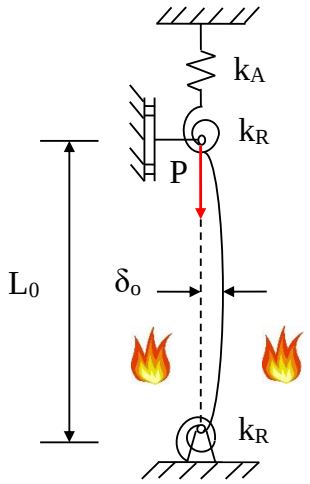

Figure 4: The simulated model of the axially and rotationally restrained columns.

2.2.3 Material modelling and geometric imperfections

The stress-strain relationship for carbon steel at elevated temperatures provided in EN 1993-1-2 [9], along with the measured room temperature material properties from [15] and the elevated temperature reduction factors set out in EN 1993-1-2 [9], were employed. The true stress σ_{true} and log plastic strain $\varepsilon_{\ln,}^{pl}$ which were derived from the engineering stress-strain responses, as defined in Equations (3) and (4), respectively, where σ_{nom} is the engineering stress, ε_{nom} is the engineering strain and E is the Young's modulus were incorporate into the numerical models.

$$\sigma_{true} = \sigma_{nom}\left(1+\varepsilon_{nom}\right) \tag{3}$$

$$\varepsilon_{\ln}^{pl} = \ln\left(1+\varepsilon_{nom}\right) - \frac{\sigma_{true}}{E} \tag{4}$$

Imperfections in the form of the lowest global and local buckling modes, obtained from a linear eigenvalue buckling analysis, were assigned to the numerical models. The global imperfection amplitude δ_0 was set to L/1000, where L is the column length [19]. The local imperfection amplitude ω_0 predicted by the modified Dawson and Walker model [20] given by Equation (5), where t is the thickness, f_y is the material yield stress and $f_{cr,min}$ is the minimum elastic buckling stress of all the plate elements making up the cross-section, was employed.

$$\omega_0 = 0.028t\left(f_y / f_{cr,\min}\right)^{1/2} \tag{5}$$

2.2.4 Residual stresses

Residual stresses in hot-rolled steel sections are associated with the differential cooling after the forming process, where the more rapidly cooling regions of the sections are found to be in residual compression, whilst the slower cooling regions are in residual tension. The residual stress pattern recommended in [21-22] for cross-sections with height-to-width ratio H/B less than or equal to 1.2, as shown in Figure 5, was applied to the FE models, where the compressive residual stresses designated as negative and the tensile residual stresses as positive were both set to $0.5f_y^*$, where $f_y^* = 235$ MPa is taken as the reference value as recommended in [21]. Residual stresses were introduced into the finite element models by partitioning the web and

flanges of each cross-section; each partition represents a stress level corresponding to the mid-point of the linear variation in stress over the partition length [23]. The stresses were applied using the *INITIAL CONDITIONS command and equilibration of the stresses was achieved through an initial linear perturbation load step. The four-noded doubly curved shell element with reduced integration (S4R) from the ABAQUS element library, with the same mesh element size as for the thermal models (10mm×10mm), was employed.

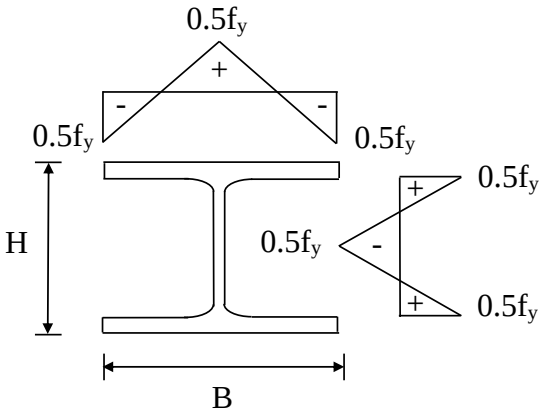

Figure 5: The residual stress pattern applied to the carbon steel I-section columns.

2.2.5 Boundary conditions and analysis steps

Boundary conditions at the columns ends were carefully selected to simulate the experimental set-up. The column end cross-sections were each connected to an eccentric reference point, with eccentricity = 1mm as used in the experiments, through *Rigid Body coupling such that the degrees of freedom of all nodes at each end were constrained to the degrees of freedom of its corresponding reference point. The bottom reference point (RP-Bottom) was offset by 30 mm representing the thickness of the end-plate, while the top reference point (RP-Top) was offset by an additional 600mm representing the depth of the measurement device – see Figure 6. The axial and rotational springs were attached to these reference points. At the bottom reference point (RP-Bottom), all degrees of freedom apart from rotation about the cross-section minor axis (R_Y=FREE) were restrained. At the top reference point (RP-Top), all degrees of freedom were restrained apart from the longitudinal translation and rotation about the cross-section minor axis (U_Z=FREE, R_Y=FREE); the initial axial load P_0 was applied to the model through this reference point.

The stress analysis was conducted in two steps. In the first step, the initial load P_0 was applied at room temperature to the top end of the column through its reference point RP-Top. In the second step, this load was maintained, while the evolution of the temperature with the fire exposure time was imported from the thermal model. The axial and rotational springs were activated at the start of the second step to measure the restraint forces induced by the restrained axial and rotational displacements. The general static solver in ABAQUS was used for both analyses steps. In the stress analysis step, where the unstable behaviour of the steel members at elevated temperatures caused numerical convergence issues, an adaptive automatic stabilisation scheme with a constant damping of 0.0002 was adopted.

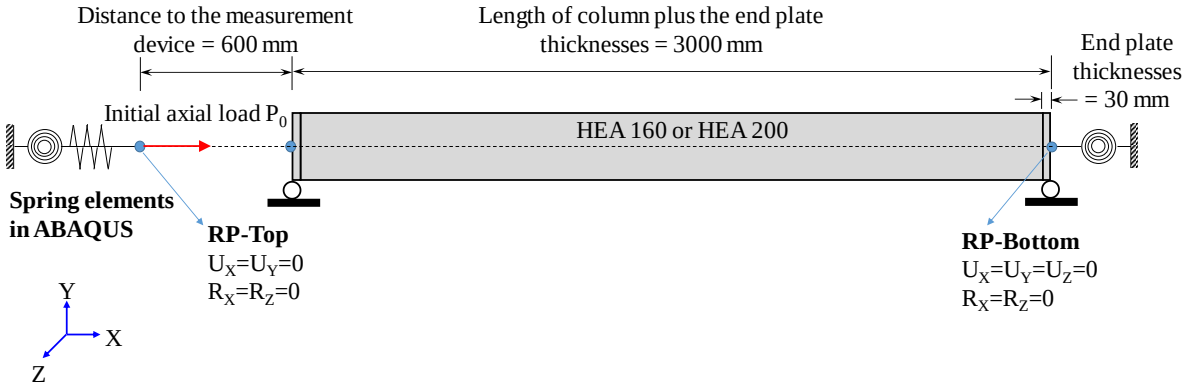

Figure 6: Definition of boundary conditions for the stress analysis model.

2.3 Validation results

A total of 12 axially and rotationally restrained steel columns were modelled using the sequentially coupled thermal-stress analysis procedure described in Section 2.2. The total axial force P in the restrained columns comprises of the initial axial force P_0 (30% or 70% of $N_{b,z,Rd}$) and the restrained thermal expansion force P_{res} due to the restrained thermal expansion strains. Figures 7-9 compare the experimental and numerical results for the normalised total axial force P/P_0 versus time, normalised total axial force P/P_0 versus temperature and column axial displacement versus temperature, respectively for the HEA200-K13-L30, HEA200-K45-L30, and HEA200-K128-L30 columns. In Figure 7, the results of the FE simulations of the tested columns by Correia et. al. [24], where the whole test frame was modelled, have also been added for comparison purposes.

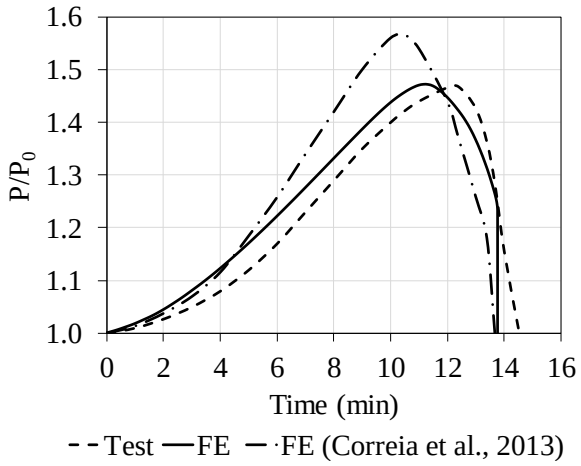

(a) HEA200-K13-L30.

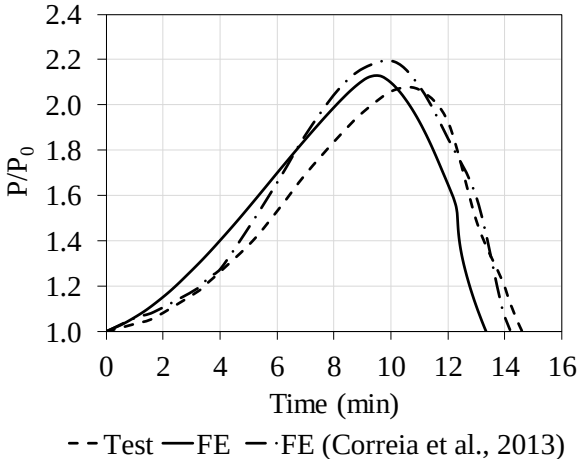

(b) HEA200-K45-L30.

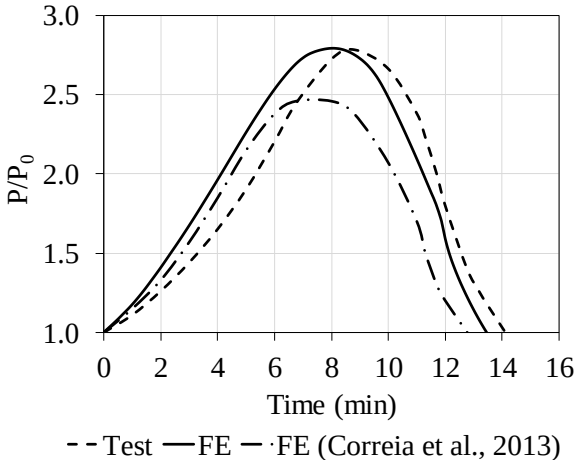

(c) HEA200-K128-L30.

Figure 7: Comparison of experimental and numerical P/P0 versus time for (a) HEA200-K13-L30, (b) HEA200-K45-L30 and (c) HEA200-K128-L30.

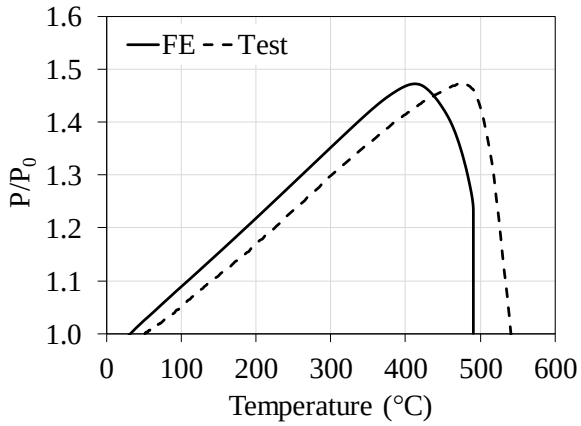

(a) HEA200-K13-L30.

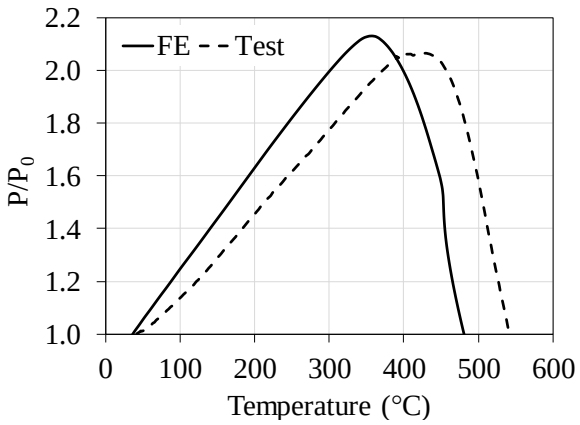

(b) HEA200-K45-L30.

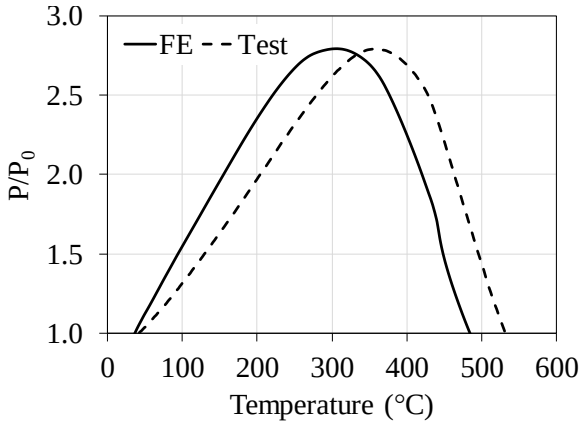

(c) HEA200-K128-L30.

Figure 8: Comparison of experimental and numerical P/P0 versus temperature for (a) HEA200-K13-L30, (b) HEA200-K45-L30 and (c) HEA200-K128-L30.

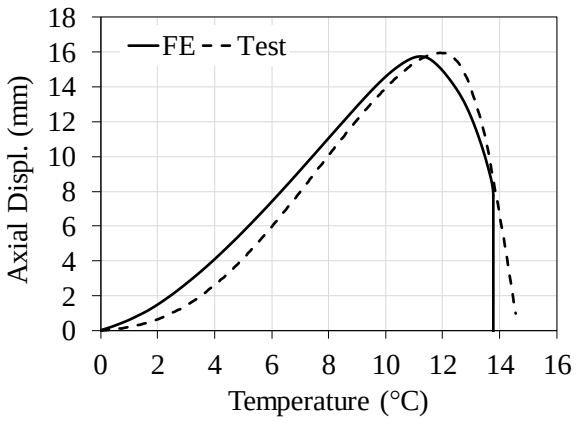

(a) HEA200-K13-L30.

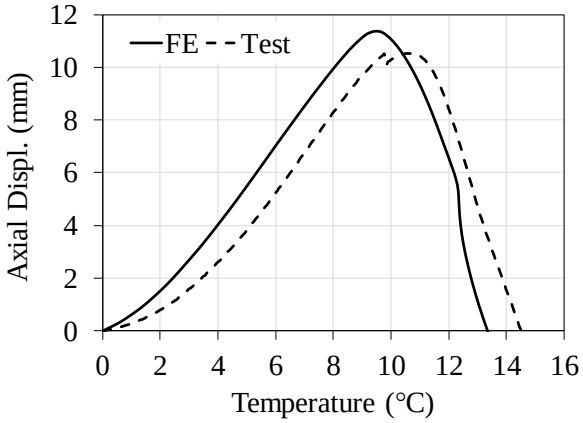

(b) HEA200-K45-L30.

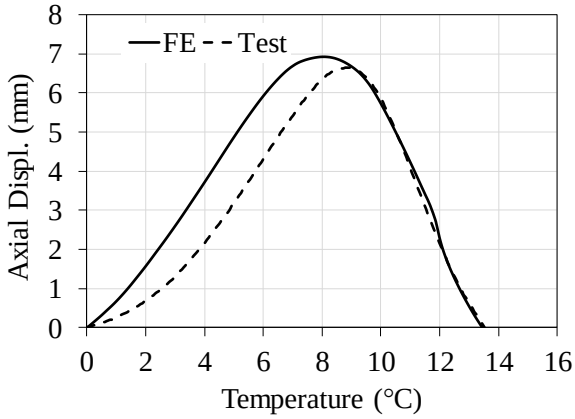

(c) HEA200-K128-L30.

Figure 9: Comparison of experimental and numerical results of column axial displacement versus temperature for (a) HEA200-K13-L30, (b) HEA200-K45-L30 and (c) HEA200-K128-L30.

A summary of the comparisons between the test and FE failure temperature and time results is provided in Table 2. The failure temperature and time were defined as the temperature and time at which the total axial force P returned to the value of the initial applied load P_0, i.e. load ratio P/P_0 approaching unity, on the descending load-temperature/time response. The average temperature was taken as the mean temperature in sections S1-S5 averaged over the column height. The average ratios of the FE-to-test failure temperature and time were 0.982 and 0.943 with corresponding coefficients of variation (COV) of 0.075 and 0.044, respectively.

The failure modes of the tested steel columns mainly included global buckling instability and in some cases cross-section local buckling instability [15]. Example failure modes for HEA160-K13-L30 and HEA200-K128-L30 columns are shown in Figure 10, which closely match those observed in the physical experiments.

Table 2: Comparison of failure temperatures and times between test and FE results.

Specimen reference	Failure time (min)			Failure temperature (°C)		
	Test	FE	FE/Test	Test	FE	FE/Test
HEA200-K13-L70	11.6	10.5	0.902	445	406	0.913
HEA160-K13-L70	10.6	10.6	0.986	428	404	0.944
HEA200-K13-L30	14.6	13.8	0.945	541	491	0.907
HEA160-K13-L30	13.6	13.6	0.999	545	497	0.912
HEA200-K45-L70	11.4	10.9	0.957	433	388	0.897
HEA160-K45-L70	10.3	10.5	1.019	416	401	0.964
HEA200-K45-L30	14.6	13.5	0.924	543	485	0.893
HEA160-K45-L30	13.2	13.3	1.010	511	493	0.964
HEA200-K128-	11.8	11.4	0.964	457	418	0.914
HEA160-K128-	9.6	9.9	1.025	404	413	1.022
HEA200-K128-	14.3	13.8	0.964	532	493	0.927
HEA160-K128-	12.9	15.5	1.202	499	510	1.021
Mean			0.982			0.943
COV			0.075			0.044

(a) Global buckling modes obtained from FE (LHS) and test (RHS) for HEA160-K13-L30 specimen.

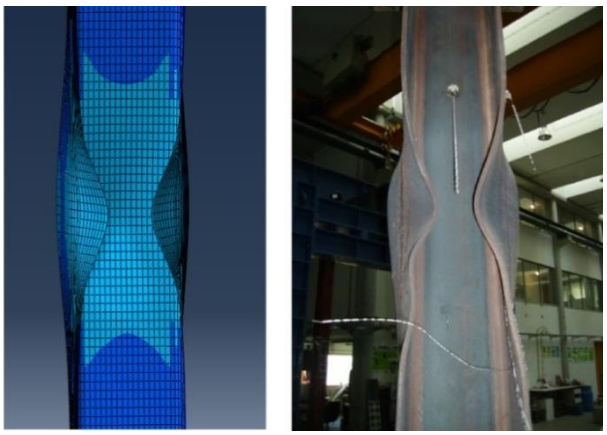

(b) Local buckling modes obtained from FE (LHS) and test (RHS) for HEA200-K128-L30 specimen.

Figure 10: Comparison of test [15] and FE failure modes.

Considering the comparisons made between the FE and the test results presented in this section, it is concluded that the FE models are capable of producing accurate, consistent and safe-side predictions of the test response and are suitable for performing parametric studies for axially and rotationally restrained stainless steel columns presented in Section 3.

3. Parametric study

Having validated the FE models, parametric studies were carried out to study the fire response of axially and rotationally restrained stainless steel columns. The key investigated parameters included: (i) axial restraint stiffness; (ii) rotational restraint stiffness; (iii) column slenderness; and (iv) load level. The applied load levels were 30%, 40%, 50%, 60% and 70% of the room temperature minor axis buckling resistance $N_{b,z,Rd}$, determined in accordance with EN 1993-1-4 [2]. The column lengths were varied to give a range of room temperature minor axis member slenderness in the range $0.5 \leq \bar{\lambda} \leq 2.0$.

For the purpose of evaluating the influence of axial and rotational restraint on the column behaviour at elevated temperature, four combinations of axial and rotational restraint stiffness ratios α_A and α_R, respectively, as summarised in Table 3, were employed. The range of the investigated axial restraint stiffness ratios were based on the studies of Lennon [25] which revealed a practical range of axial restraint stiffness α_A between 0.05 and 0.35 depending on the column position in buildings. The studied rotational restraint stiffness ratios corresponded to low, medium and high levels of rotational restraint, as adopted in a similar study by Faris and O'Connar [26].

Table 3: Axial and rotational stiffness ratios adopted for FE parametric study.

Combination	Rotational restraint stiffness ratio α_R		Axial restraint stiffness ratio α_A
1	Zero	$\alpha_R = 0$	α_A = 0.002-0.35
2	Low	$\alpha_R = 0.2$	α_A = 0.02-0.30
3	Medium	$\alpha_R = 0.5$	α_A = 0.02-0.30
4	High	$\alpha_R = 0.9$	α_A = 0.02-0.30

The same modelling procedures as explained in Section 2 were employed for the parametric study models with the input parameters for stainless steel taken as those as described hereafter. The cross-section employed for all parametric study models was I-102×68×5×5 with height, width, web thickness and flange thickness equal to 102 mm, 68 mm, 5 mm and 5 mm, respectively. The selected cross-section is classified as Class 1 according to EN 1993-1-4 [2].

The room temperature material properties for hot-rolled austenitic stainless steel plates recommended by Afshan et al. [19] for numerical parametric studies of stainless steel structural elements, reported in Table 4, were employed. In Table 4, E is the Young's modulus, f_y is the yield stress taken as the 0.2% proof stress, f_u is the ultimate tensile stress, ε_u is the strain at the ultimate tensile stress and n and m are the two-stage Ramberg-Osgood model parameters. The reduction factors pertaining to grade EN 1.4571 provided in *Table 8.1* of the Design Manual for Structural Stainless Steel [8] were employed. The two-stage Ramberg-Osgood model given by Equations 6 and 7 was employed to construct full range stress-strain curves which were input into the FE models in the form of true stress and log-plastic strain.

$$\varepsilon_\theta = \frac{\sigma_\theta}{E_\theta} + 0.002\left(\frac{\sigma_\theta}{f_{y,\theta}}\right)^{n_\theta} \quad \text{for } \sigma_\theta \le f_{y,\theta} \tag{6}$$

$$\varepsilon_\theta = \frac{\sigma_\theta - f_{y,\theta}}{E_{0.2,\theta}} + \varepsilon_{u,\theta}\left(\frac{\sigma_\theta - f_{y,\theta}}{f_{u,\theta} - f_{y,\theta}}\right)^{n_\theta} + \varepsilon_{y,\theta} \quad \text{for } f_{y,\theta} < \sigma_\theta \le f_{u,\theta} \tag{7}$$

where σ_θ and ε_θ are the stress and strain, respectively at temperature θ, $f_{y,\theta}$ is the yield stress, taken as the 0.2% proof stress, at temperature θ, E_θ is the Young's modulus at temperature θ, $E_{0.2,\theta}$ is the tangent modulus at $f_{y,\theta}$, $\varepsilon_{y,\theta}$ is the total strain corresponding to $f_{y,\theta}$, $\varepsilon_{u,\theta}$ is the strain at ultimate tensile stress $f_{u,\theta}$ and n_θ and m_θ are the Ramberg-Osgood model parameters at temperature θ.

Table 4: Material properties of EN 1.4571 stainless steel grade at room temperature.

Stainless steel	E (N/mm^2)	f_y (N/mm^2)	f_u (N/mm^2)	ε_u	n	m
EN 1.4571	200000	280	580	0.5	9.1	2.3

The standard ISO 834 temperature-time curve given in EN 1993-1-2 [9] was used for the thermal model. The convective heat transfer coefficient factor and the emissivity were taken as 25 $W/(m^2\ °C)$ and 0.4, respectively, as specified in EN 1993-1-2 [9]. Thermal properties including specific heat, thermal expansion and thermal conductivity as recommended in [8] for austenitic stainless steels were employed. The global imperfection amplitude was set to *L/1000* for all stainless steel columns, where *L* is the column length. The local imperfection amplitudes ω_0 were determined by means of the Dawson and Walker model, as adapted for stainless steel [27], as given by Equation (8), where the parameters are as previously defined in Section 2.2.3.

$$\omega_0 = 0.023t\left(f_y / f_{cr,\min}\right) \tag{8}$$

The residual stress patterns associated with laser welded stainless steel I-sections were incorporated into the FE models. Laser welding which has been shown to offer the potential for a greater degree of automation, with higher welding speeds, quality and precision has been used for production of mild steel and stainless steel sections [28]. The magnitude and distribution of residual stresses in the laser-welded stainless steel sections were studied experimentally by Gardner et al. [28], and predictive models were proposed as shown in Figure 11, which was adopted in the numerical parametric models developed herein. In Figure 11, the maximum tensile residual stresses in the web f_{wt} and the flange f_{ft} were both set to $0.5f_y$, the maximum compressive residual stresses in the web f_{wc} and the flange f_{fc} were then obtained from equilibrium and the parameters *a*, *b*, *c*, and *d* were set to $0.1b_f$, $0.075b_f$, $0.025h_w$, and $0.05h_w$, respectively [28].

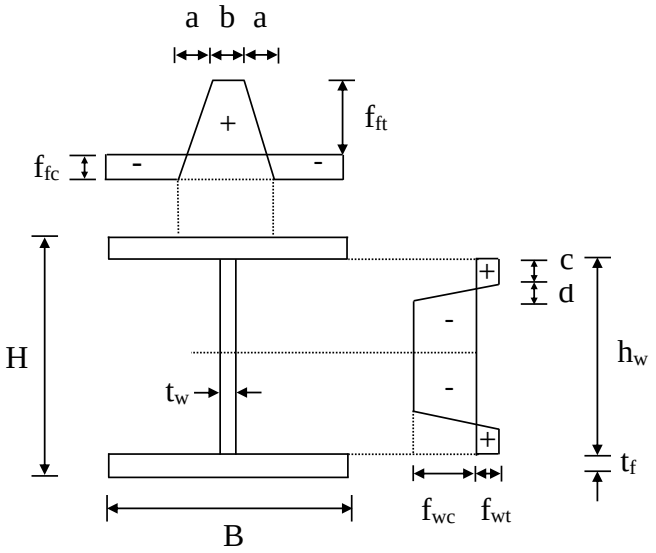

Figure 11: The residual stress pattern applied to the laser welded stainless steel I-section columns from [28].

4. Analyses of results and discussions

4.1 Axially restrained and rotationally unrestrained columns

The fire performance of axially restrained and rotationally unrestrained stainless steel columns is discussed in this section. When considering the behaviour of an axially restrained column, it is important to distinguish between the column buckling temperature θ_b and the column failure temperature θ_f [29]. The buckling temperature θ_b is defined as the temperature at which the axial load in the column reaches its maximum value P_{max} – see Figure 12 [29]. Since after buckling the axial load in a restrained column reduces, the failure temperature θ_f is defined as the temperature at which the axial load returns to its original value P_0 – see Figure 12 [29].

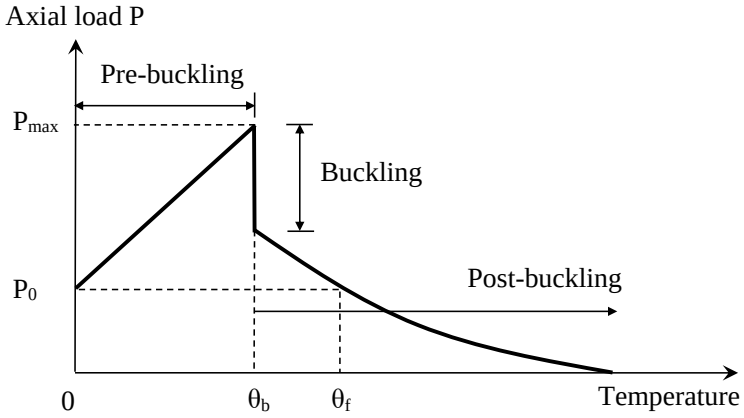

Figure 12: Stages of behaviour of a restrained column when subjected to fire [29].

Two types of failure responses were observed for the axially restrained stainless steel columns modelled herein – Type-I response where the column failure temperature θ_f equals the buckling

temperature θ_b with little or no post-buckling response and Type-II response where the column failure temperature θ_f exceeds the buckling temperature θ_b, as shown in Figure 13. Type-I response was observed for restrained stainless steel columns with low degrees of axial restraint stiffness, while Type-II response was exhibited by those with higher degrees of axial restraint stiffness.

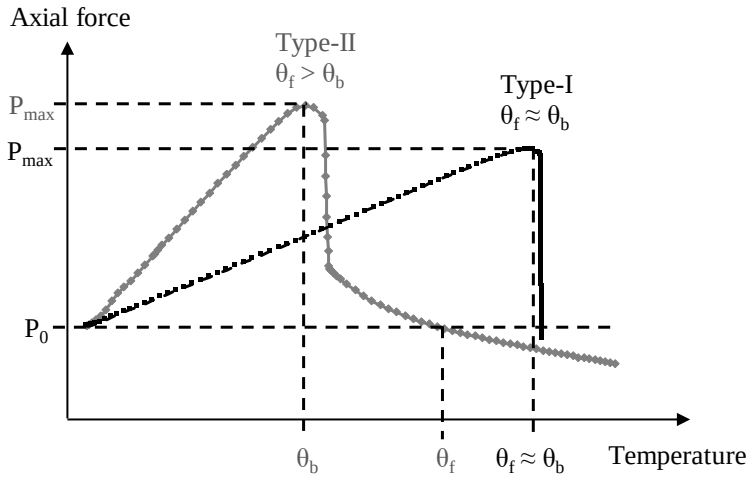

Figure 13: Two types of responses of restrained stainless steel columns from FE models.

Figure 14 shows the variation of the failure temperature θ_f with the axial restraint stiffness ratio α_A and applied load level for columns with member slenderness $\overline{\lambda}$ = 0.75 and 1.5. As shown in Figures 14(a) and (b), the failure temperature θ_f decreases with increasing axial restraint stiffness ratio α_A, demonstrating the detrimental effect of the additional axial force generated from the restrained thermal expansion. As expected, for a given column slenderness, the failure temperature θ_f is lower for higher applied load levels, as shown in Figures 14(c) and (d). As illustrated in Figures 14(a)and (b) there is a limiting axial restraint stiffness ratio beyond which there is no further reduction in the failure temperature with increasing axial restraint stiffness. This limiting restraint ratio is in fact a branching point that divides Type-I and Type-II response modes of axially restrained columns in fire (i.e. where the post-buckling response becomes significant). The value of the limiting α_A depends on the applied load level, and the column slenderness. For example, as shown in Figure 14(a) and (b), for the columns with $\overline{\lambda}$ = 0.75, for load level of 30%, this limiting axial restraint stiffness ratio is 0.1, while for the load level of 70%, it is 0.25, while for the columns with $\overline{\lambda}$ = 1.5, these are 0.05 and 0.2 for 30% and 70% applied load levels, respectively. Therefore, the limiting axial restraint stiffness ratio increases with increasing load level and reduces with increasing slenderness.

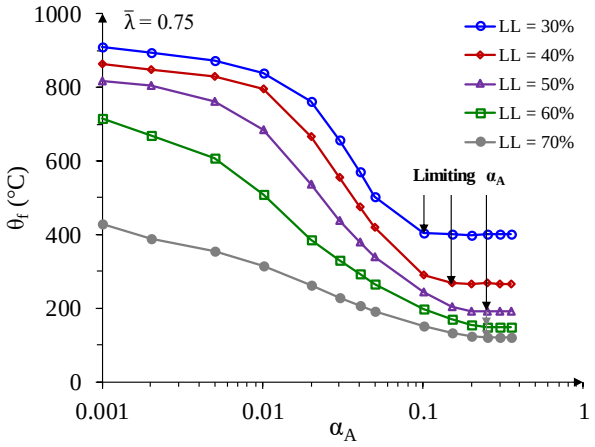

(a) Effect of axial restraint stiffness for $\bar{\lambda}$=0.75.

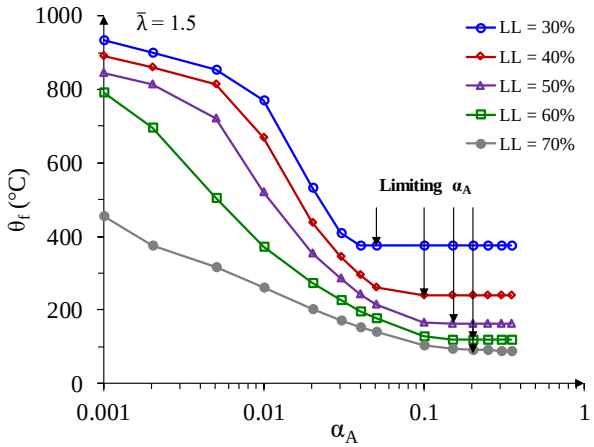

(b) Effect of axial restraint stiffness $\bar{\lambda}$=1.5.

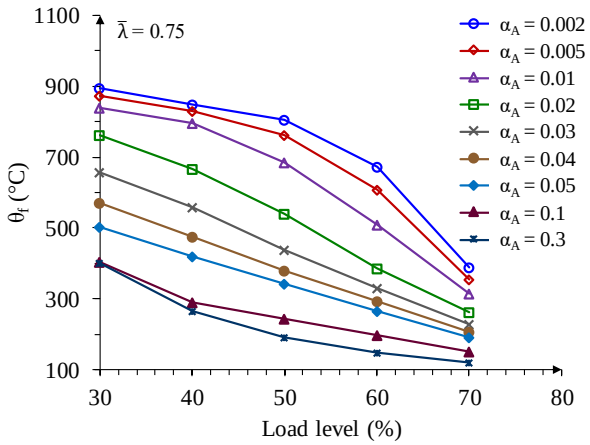

(c) Effect of axial load level for $\bar{\lambda}$=0.75.

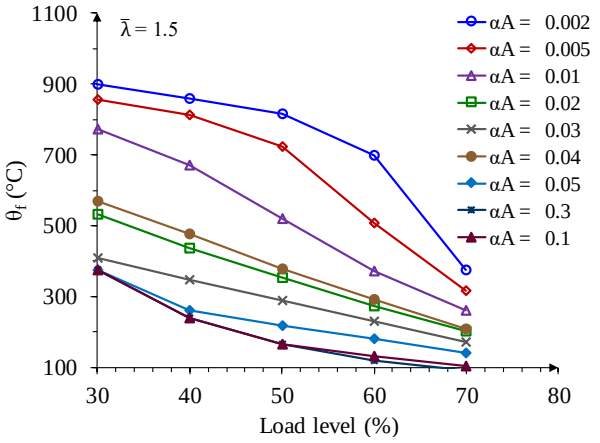

(d) Effect of axial load level for $\bar{\lambda}$=1.5.

Figure 14: Effect of axial restraint stiffness and axial load level on the failure temperature of axially restrained column.

Figure 15 shows the variation of the failure temperature θ_f with the column slenderness $\bar{\lambda}$ for the modelled stainless steel columns for three levels of α_A equal to 0.002, 0.02 and 0.2. The failure temperature θ_f reduces with increasing column slenderness $\bar{\lambda}$ for all axial restraint stiffness ratios. The higher reduction in θ_f exhibited by the intermediate slenderness range columns, i.e. $\bar{\lambda}$ = 0.5-1.25, is due to the greater reduction in the stiffness of the columns as also observed by [18] and [30].

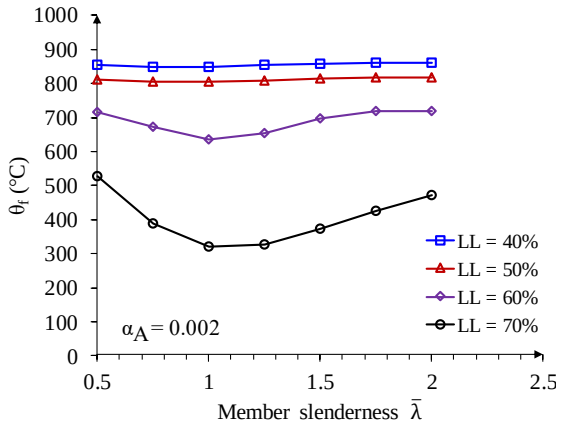

(a) α_A= 0.002.

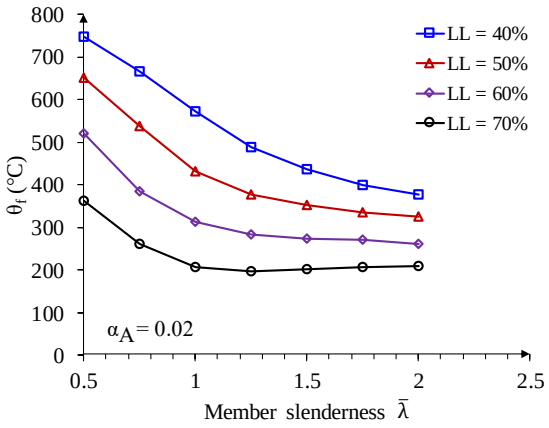

(b) α_A= 0.02.

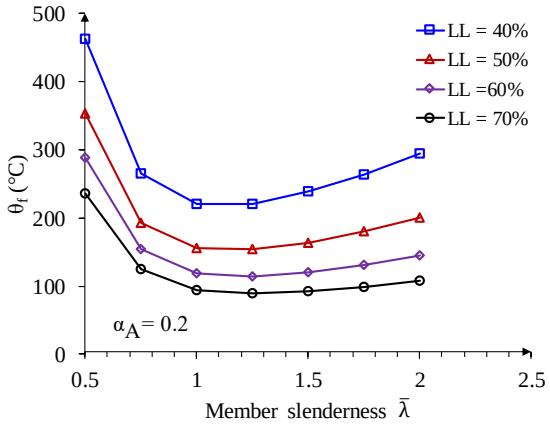

(c) α_A= 0.2.

Figure 15: Effect of column slenderness on the failure temperature of axially restrained column.

The difference between the failure temperature θ_f and the buckling temperature θ_b of the modelled axially restrained stainless steel columns versus the axial restraint stiffness ratio α_A is shown in Figures 16(a) for columns with $\bar{\lambda}$ = 1.50. For columns with low axial restraint stiffness ratios (α_A < 0.02-0.03 for this case), the difference in the temperatures $(\theta_f - \theta_b)$ is very small for all the considered load levels, as the columns exhibit predominantly Type-I response. However, this difference $(\theta_f - \theta_b)$ increases with increasing axial restraint stiffness ratio, where the columns show Type-II response, and is higher for lower load levels. This means that for columns where the axial restraint stiffness is low (α_A < 2–3%) and the applied load level is high there is little benefit in considering the post-buckling behaviour. Figure 16(b) show the variation of $(\theta_f - \theta_b)$ with the column slenderness $\bar{\lambda}$ for the modelled stainless steel columns under the applied load level equal to 70%. For the low to intermediate slenderness range ($\bar{\lambda}$ = 0.5-1.25), the difference in the temperatures $(\theta_f - \theta_b)$ reduces with increasing slenderness, while in the high slenderness range ($\bar{\lambda}$ >1.25), it increases with increasing slenderness. Therefore, with a combination of low initial load level, high column slenderness and high restraint stiffness, the column failure temperature can be much higher than its buckling

temperature. Therefore, the column post-buckling response may be considered in the fire design of axially restrained columns, if large structural deformations in fire are allowed.

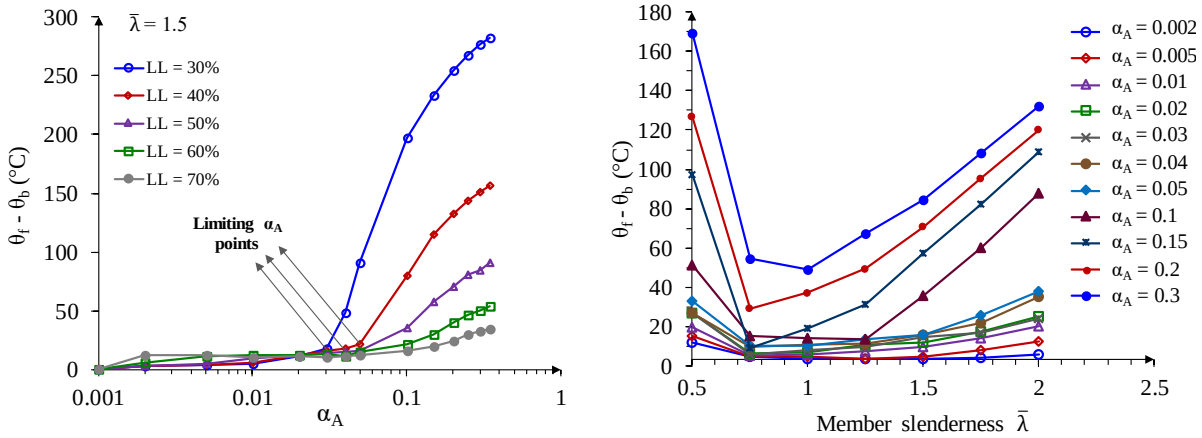

(a) (b)

Figure 16: Variation of (θ_f-θ_b) with (a) axial restraint stiffness ratio and (b) column slenderness.

4.2 Axially and rotationally restrained columns

The normalised axial force P/P_0 versus temperature responses for the stainless steel columns ($\bar{\lambda}$ = 1.0) with both axial and rotational restraints subjected to 70% load level are shown in Figure 17. As illustrated in Figure 17, for a given axial restraint stiffness ratio (e.g. α_A = 0.02, 0.05, 0.1, 0.2 and 0.3), increasing the degree of the rotational stiffness ratio (e.g. from α_R = 0.2 to 0.5 and 0.9), the performance of the columns, in terms of both the maximum load reached and the failure temperature, improves. The observed increase in the maximum load carrying capacity and the failure temperature θ_f of the columns with the increasing levels of rotational restraint stiffness ratio α_R is associated with the reduction in the maximum bending moments in the highly stressed mid-height cross-section of the columns since the column ends, with some degree of rotational fixity, begin to attract some of the applied bending moments as the temperature increases.

Figures 18 shows the variation of the failure temperature θ_f with the rotational restraint stiffness ratio α_R for the modelled stainless steel columns under 50% and 70% applied load levels. For a given column slenderness $\bar{\lambda}$ and axial restraint ratio α_A, increasing the level of rotational stiffness ratio α_R increases the column failure temperature θ_f. This increase in the failure temperature is greatest for lower slenderness columns and columns with lower axial restraint stiffness ratios. The effect of the presence of rotational restraint stiffness is more significant at higher applied load levels. Therefore, while increasing the level of axial restraint stiffness was shown to generally reduce the failure temperature of the stainless steel columns in fire, introduction of rotational restraints and increasing the level of rotational restraint stiffness was shown to effectively have the opposite effect.

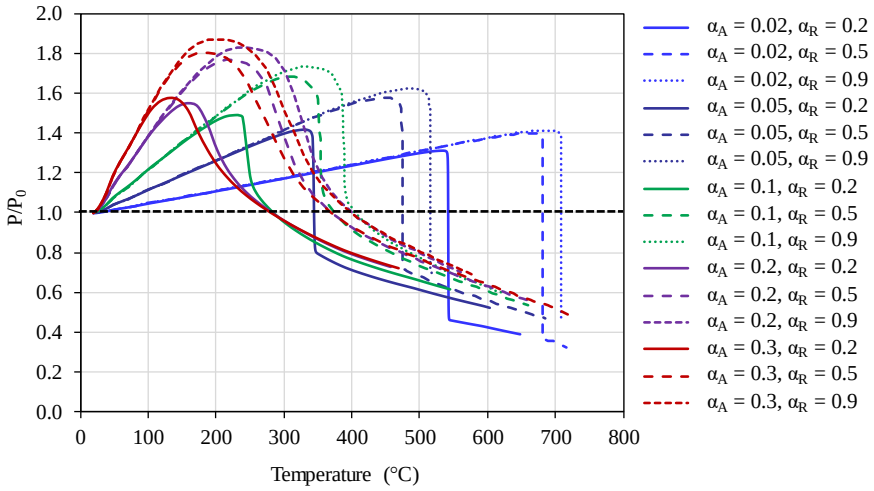

Figure 17: Normalised load versus temperature responses for axially and rotationally restrained columns with $\bar{\lambda}$ = 1.0 and 70% load level.

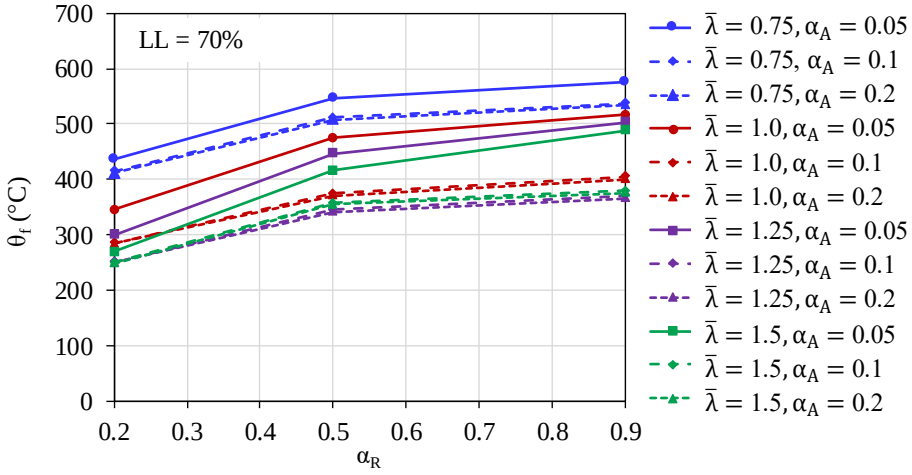

(a)

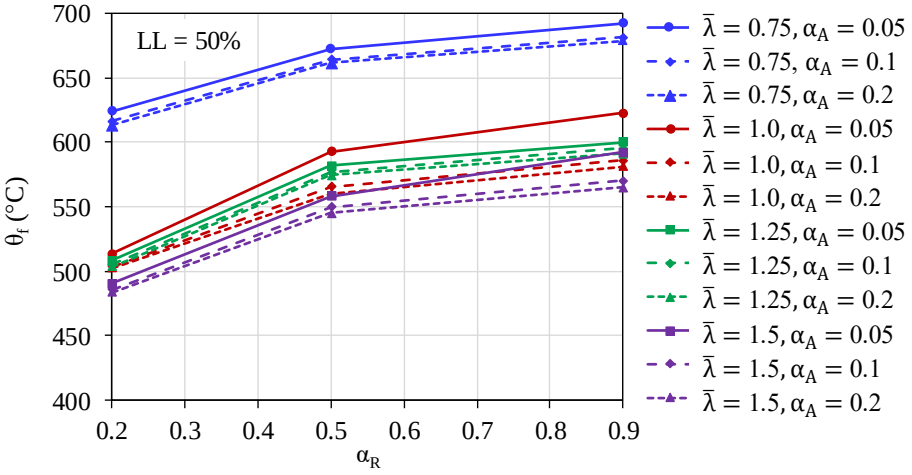

(b)

Figure 18: Effect of combined axial and rotational restraint stiffness on the critical temperature (a) load level = 70% and (b) load level = 50%.

5. Conclusion

To assess the response of axially and rotationally restrained stainless steel columns in fire, a numerical modelling study is conducted. A total of twelve fire tests on axially and rotationally restrained carbon steel columns from the literature are replicated using the finite element analysis package ABAQUS to obtain a validated numerical modelling procedure. The development of the models, including thermal analysis models, linear eigenvalue buckling analysis models and stress analysis models is described in detail. Parametric studies to explore the influence of the variations in (i) axial restraint stiffness, (ii) rotational restraint stiffness, (iii) column slenderness and (iv) load level are described. For axially restrained and rotationally unrestrained stainless steel columns, it is shown that the failure temperature θ_f decreases with increasing axial restraint stiffness ratio α_A due to increased thermally-induced axial stresses. There is a limiting restraint ratio beyond which the failure temperature no longer reduces with the axial restraint stiffness increments. This same limiting restraint ratio is also a branching point that divides Type-I and Type-II failure modes (i.e. where the post-buckling response becomes significant). For axially restrained and rotationally restrained stainless steel columns, increments in the rotational restraint stiffness are shown to increase the failure temperature of the stainless steel columns, reflecting their function to effectively redistribute the thermal stresses away from the mid-span. Future work will focus on the development of a design method for stainless steel columns in fire taking into consideration the influences of axial and rotational restraint stiffness on the column failure mode and the failure temperature taking also into consideration the observed post-buckling response.

Acknowledgements

The financial support provided by the Institution of Civil Engineers (ICE), through the ICE Research and Development Enabling Fund, and Brunel University London, through the BRIEF research fund under grant LBL354, is gratefully acknowledged.

References

1. Baddoo N.R. 100 years of stainless steel: A review of structural applications and the development of design rules. *The Structural Engineer*, 2013; 91: 10-18.
2. EN 1993-1-4. Eurocode 3: Design of Steel Structures – Part 1.4: General Rules Supplementary Rules for Stainless Steels. Brussels: European Committee for Standardization (CEN), 2015.
3. AISC Design Guide 27: Structural Stainless Steel. American Institute of Steel Construction, 2013.
4. CECS-410. Technical Specification for Stainless Steel Structures. China Planning Press, Beijing, 2015 (in Chinese).
5. A.S/N.Z.S. 4673. Cold-Formed Stainless Steel Structures. Standards Australia, Sydney, 2001.
6. Gardner L. Stainless steel structures in fire. *Proceedings of the Institution of Civil Engineers – Structures and Buildings*, 2007; 160(3): 129-138.
7. Huang Y., Young B. Stress-strain relationship of cold-formed lean duplex stainless steel at elevated temperatures. *Journal of Constructional Steel Research, 2014;* 92: 103-113.

8. Design Manual for Structural Stainless Steel. Fourth Edition. SCI Publication No. P413. The Steel Construction Institute, UK, 2017.
9. EN 1993-1-2. Eurocode 3: Design of Steel Structures - Part 1.2: General Rules – Structural Fire Design. Brussels: European Committee for Standardization (CEN), 2005.
10. Uppfeldt B., Ala Outinen T. and Veljkovic M. A design model for stainless steel box columns in fire. *Journal of Constructional Steel Research*, 2008; 64: 1294-1301.
11. Lopes N., Vila Real P., Simões da Silva L.S. and Franssen J.M. Numerical analysis of stainless steel beam-columns in case of fire. *Fire Safety Journal*, 2012; 50: 35-50.
12. Usmani A.S., Rotter J.M., Lamont S., Sanad A.M. and Gillie M. Fundamental principles of structural behaviour under thermal effects. *Fire Safety Journal*, 2001; 36(8): 721-744.
13. Lamont S., Lane B., Flint G., and Usmani A.S. Behaviour of structures in fire and real design – A case study. *Journal of Fire Protection Engineering*, 2006; 16: 5-35.
14. ABAQUS. 2015. ABAQUS, version 2016. Simulia, Dassault Systèmes, 2015.
15. Correia A.M. and Rodrigues J.P.C. Fire resistance of steel columns with restrained thermal elongation. *Fire Safety Journal*, 2012; 50: 1-11.
16. Huang Z.F. and Tan K.H. Structural response of restrained steel columns at elevated temperatures. Part 2: FE simulation with focus on experimental secondary effects. *Engineering Structures*, 2007; 29: 2036-2047.
17. Jiang B. Li G.Q. and Izzuddin B.A.Dynamic performance of axially and rotationally restrained steel columns under fire. *Journal of Constructional Steel Research*, 2016; 122: 308-315.
18. Wang P. Wang Y. and Li G.Q. Behaviour and design of restrained steel column in fire: Part 2. Parameter study. *Journal of Constructional Steel Research*, 2010; 66: 1148-1154.
19. Afshan S., Zhao O. and Gardner L. Standardised material properties for numerical parametric studies of stainless steel structures and buckling curves for tubular columns. *Journal of Constructional Steel Research*, 2018; 152: 2-11.
20. Dawson R.G. and Walker A.C. Post-buckling of geometrically imperfect plates. *Journal of the Structural Division (ASCE)*, 1972; 98(1): 75-94.
21. ECCS. Ultimate limit state calculation of sway framed with rigid joints. Technical Committee 8 (TC 8) of European Convention for Constructional Steelwork (ECCS), Tech. Rep. No. 33, 1984.
22. Yun X., Gardner L. and Boissonnade N. The continuous strength method for the design of hot-rolled steel cross-sections. *Engineering Structures*, 2018; 157: 179-191.
23. Foster A.S.J. and Gardner L. Ultimate behaviour of continuous steel beams with discrete lateral restraints. *Thin-Walled Structures*, 2015; 88: 58-69.
24. Correia A.J.P.M., Rodrigues J.P.C. and Gomes F.C.T. A simplified calculation method for fire design of steel columns with restrained thermal elongation. *Computers and Structures*, 2013; 116: 20-34.
25. Lennon T. Local column heating fire. *Cardington Conference, Building Research Establishment*, UK, 1994.
26. Ali F. and O'Connor D. Structural performance of rotationally restrained steel columns in fire. *Fire Safety Journal*, 2001; 36: 679–691.

27. Ashraf M., Gardner L. and Nethercot D.A. Finite element modelling of structural stainless steel cross-sections. *Thin-walled structures,* 2006; 44(10): 1048-1062.

28. Gardner L., Bu Y. and Theofanous M. Laser-welded stainless steel I-sections: Residual stress measurements and column buckling tests. *Engineering Structures, 2016; 127: 536-548.*

29. Wang Y.C. *Steel and Composite Structures: Behaviour and Design for Fire Safety*, SPON Press, London and New York, 2002.

30. Wang Y.C. Post-buckling behaviour of axially restrained and axially loaded steel columns under fire conditions. *Journal of Structural Engineering*, 2004; 130(3): 371-380.